Strong-field approximation for the wavelength scaling of high-harmonic generation

Dane R. Austin[1] and Jens Biegert[1,2]
[1]*Institut de Ciencies Fotoniques, Mediterranean Technology Park, 08860 Castelldefels, Barcelona, Spain*
[2]*Institució Catalana de Recerca i Estudis Avançats, 08010 Barcelona, Spain*

(Received 15 February 2012; revised manuscript received 8 June 2012; published 7 August 2012)

We derive analytic expressions for the spectral amplitude of high-order harmonic generation from a single atom using the strong-field approximation (SFA). We demonstrate good agreement with time-dependent Schrödinger equation calculations, including the dependence on the drive wavelength across the range 566–2260 nm. Previous claims of a discrepancy in the drive wavelength scaling ignore changes in the timing of trajectories corresponding to a fixed harmonic photon energy. Under this condition, tunnel ionization is shown to play the most important role for the short trajectories. The established agreement enables us to use the SFA to predict that the intensity at the classical cutoff scales inversely with the ninth power of the drive wavelength in the high photon energy limit when the Coulomb singularity dominates the recombination amplitude.

DOI: 10.1103/PhysRevA.86.023813 PACS number(s): 42.65.Ky, 42.65.Re, 42.55.Vc

I. INTRODUCTION

In the semiclassical picture of high-harmonic generation (HHG), the electric field of a strong laser pulse pulls an electron away from an atom or molecule before driving it back into the resulting ion, all within a single optical cycle [1]. The resulting collision produces extreme ultraviolet and soft-x-ray radiation with near-perfect spatial coherence [2] and subfemtosecond temporal structure [3] and is thus an attractive and compact source for extreme time-resolved spectroscopy and microscopy. For these applications, HHG is limited by its overall weak intensity and the achievable range of photon energies with which useful radiation can be generated — typically below 100 eV for common Ti:sapphire laser systems.

The well-verified three-step model [1] predicts that the maximum photon energy is $\omega_c = I_p + 3.17U_p$, where I_p is the ionization potential, $U_p = E_L^2/(4\omega_L^2)$ is the ponderomotive energy, E_L is the laser field amplitude, and ω_L is the laser frequency (all in atomic units). The laser intensity cannot be arbitrarily increased due to the phase mismatch caused by the free-electron plasma [4], as well as depletion of the ground state [5]. Therefore, much consideration has been given to extending the cutoff energy ω_c by increasing the laser wavelength [6]. By doing so, the cutoff can be extended into the biologically significant water window (284–540 eV) and beyond while preserving a sufficiently low free-electron density to retain phase matching [7]. The chirp of the attosecond bursts, a barrier to pulses shorter than the atomic unit of time, is also reduced [8].

In this context, the wavelength scaling of the yield is paramount. Although general yield calculations are complex, a simple upper bound which is also experimentally approachable is the case of phase-matched generation up to the absorption limit [9], in which the yield is the ratio of the single-atom response to the single-atom absorption. The decreasing absorption of helium and neon above 100 eV is the key for the generation of usefully bright harmonics in the x-ray region [7]. The scaling of the single-atom response is, however, still under investigation. Time-dependent Schrödinger equation (TDSE) calculations of the spectral intensity as a function of drive wavelength λ_L at constant harmonic frequency ω, constant laser intensity, and constant number of laser optical cycles, conditions we henceforth refer to as fixed absolute energy (FAE), have shown rough agreement with a power law $\lambda_L^{-\epsilon}$ [10,11] where $4.8 < \epsilon < 6$, depending on the intensity and choice of model atom. Measurements of the same quantity have given $6.3 < \epsilon < 6.6$ [12]. However, the quantum version of the three-step model, or strong-field approximation (SFA) [13], is commonly taken to imply that the same quantity goes as λ_L^{-3} around the cutoff region [14–16] or λ_L^{-4} in the plateau [14]. These factors follow from dimensional analysis of the transverse and longitudinal spreading of the electron wave packet as it undergoes a trajectory of a duration which scales as λ_L and, in the plateau, the attosecond chirp [14].

The apparent discrepancy [15,17] between the TDSE and the SFA is troubling, given the latter's ability to intuitively and accurately describe other aspects of HHG such as the time-frequency distribution [10]. The SFA remains the primary theoretical tool for designing new sources with longer drive wavelengths [7]. For the latter, predicting the performance of new systems requires knowledge of the scaling of the harmonic intensity at (varying) frequencies corresponding to a constant fraction of the ponderomotive energy, i.e., with fixed relative energy (FRE) $\bar{\omega} = (\omega - I_p)/U_p$, where $0 < \bar{\omega} < 3.17$ is the interval below the classical cutoff.

An additional concern raised by this apparent discrepancy is that the SFA, combined with the quantum path picture or equivalently the use of stationary phase approximations (SPAs), provides the framework for interpreting HHG spectra, as well as closely related photoelectron spectra. These spectra encode information on the dynamical structure of the target with subfemtosecond temporal resolution and sub-Angström spatial resolution. The signatures of ultrafast nuclear motion [18,19], electron rearrangement, and molecular orbital rearrangement [20] have all been decoded using the SFA.

Here, we show by direct comparison that the SFA accurately reproduces TDSE results for the drive wavelength scaling of HHG. Using stationary phase approximations, we present a form of the SFA that makes all scaling mechanisms explicit. This enables us to use the SFA to predict that the spectral intensity under the FRE condition goes as λ_L^{-7} times the dipole acceleration matrix element, whose additional contribution tends towards λ_L^{-2} in the high photon energy limit. The discrepancy occurs because the dimensional argument ignores

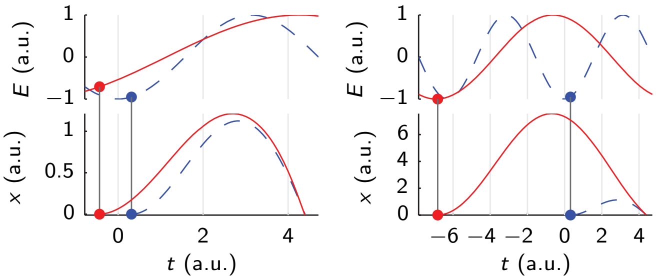

FIG. 1. (Color online) Classical electron position x (bottom row) in sinusoidal electric fields (top row) of unit amplitude and frequencies $\omega_L = 1$ a.u. (blue dashed lines) and $\omega_L = 0.5$ a.u. (red solid lines). The left (right) column shows short (long) trajectories of the red field; both columns show the cutoff trajectory of the blue field. For the purposes of illustration, we choose the relative phase of the fields (whose periods differ by a factor of 2) so that the recombination times of the trajectories coincide. The trajectories of the red field are chosen to have recombination kinetic energy equal to the cutoff of the blue field. Electron birth events are indicated by dots.

timing changes of the classical trajectories relative to the optical cycle which occur under the FAE condition:

(1) The trajectory duration, which determines the amount of wave-packet spreading, does not vary linearly with drive wavelength. Instead, the situation is as depicted in Fig. 1, which shows classical trajectories of identical recombination energy in two sinusoidal fields whose wavelengths differ by a factor of 2. The duration of the short trajectory (left column) in the longer-wavelength field (red solid lines) is much less than twice that in the shorter-wavelength field (blue dashed lines). The situation is reversed for the long trajectories (right column); the trajectory duration in the long-wavelength field is more than double that in the short-wavelength field. To generalize, with increasing drive wavelength, short trajectories become shorter relative to the optical cycle, and long trajectories become longer. Wave-packet spreading therefore only weakly affects the short trajectories, but the long trajectories suffer an attenuation even greater than λ_L^{-3}.

(2) The phase of electron birth within the optical cycle also changes. For the long trajectories, it tends slowly towards peaks of the laser field, while for the short it tends more rapidly towards zero crossings, as depicted by the dots in Fig. 1. Therefore, the tunnel ionization rate at the birth of the short trajectories drops dramatically. This is the primary scaling mechanism for the short trajectories.

In the following sections of the paper, we develop expressions for the single-atom spectral amplitude using the SFA (Secs. II and III), the accuracy of which we then establish by direct comparison with the TDSE across a wide wavelength range (Sec. IV). Next, we examine the scaling physics under the FAE energy condition (Sec. V) and present a universal scaling factor which encapsulates continuum wave-packet effects for any quasisinusoidal field (Sec. VI). We consider the FRE condition (Sec. VII) before concluding (Sec. VIII).

II. ANALYTIC SPECTRAL AMPLITUDE

To quantify the observations made in Sec. I, we derive an expression for the spectral amplitude of the single-atom response using stationary phase approximations (SPAs). We consider an arbitrary laser field profile, assuming only that solutions to the classical recollision equation are known. We shall work with two levels of approximation. The first, presented in this section, uses straightforward second- and third-order SPAs in order to evaluate the contribution to the spectral amplitude of a short, long, or cutoff trajectory in isolation. The resulting expressions transparently expose all the scaling mechanisms. However, for plotting harmonic spectra they are inadequate because they do not take into account coalescence of the trajectories at the cutoff. We rectify this by using the uniform approximation to derive more complex but generally applicable expressions. These are derived in Sec. III.

We begin with the temporal dipole response under the SFA [13,21], given by $D(t) = a(t)\exp[iS(t)]$ where

$$a(t) = g(t_b(t)) f(t_b(t)) \left[\frac{2\pi i}{\tau(t)}\right]^{3/2} g^*(t) d(v(t)). \tag{1}$$

Here, $g(t)$ is the ground-state amplitude at time t, and $t_b(t)$, $\tau(t)$, and $v(t)$ are the respective birth time, trajectory duration, and recombination electron velocity corresponding to recombination at time t, obtained from solving the classical recollision equation with zero birth velocity. The solutions are real-valued and coalesce at the cutoff. The corresponding action $S(t)$ is given by

$$S(t) = -\int_{t_b(t)}^{t} \frac{v(t_b(t),t')^2}{2} + I_p dt', \tag{2}$$

where $v(t_b,t)$ is the velocity at time t of an electron born with zero velocity at time t_b.

The zero-transverse-momentum component of the launched wave packet is [21]

$$f(t) = -\frac{(2I_p)^{1/4}}{|E(t)|}\sqrt{\frac{w(t)}{\pi}}, \tag{3}$$

where I_p is the ionization potential, $E(t)$ is the laser electric field, and $w(t)$ is the instantaneous ionization rate. For this we use the Yudin-Ivanov model [22] to take into account multiphoton and quasistatic tunneling, finding that this gives better agreement than the Ammosov-Delone-Krainov formula, especially for Keldysh parameters above 0.5. For the dipole transition element $d(v)$, we begin with the acceleration form for accuracy [21] but transform to dipole velocity because the latter is what produces the observed field [23]; the result is $d(v) = i(v^2/2 + I_p)^{-1}\langle 0| - \partial_x V|v\rangle$.

We evaluate the Fourier transform $\tilde{D}(\omega)$ of $D(t)$,

$$\tilde{D}(\omega) = (2\pi)^{-1/2}\int a(t)e^{i\phi(t)}dt, \tag{4}$$

using a stationary phase approximation (SPA). Here $\phi(t) = S(t) + \omega t$ is the action including the photon phase. We emphasize that $|\tilde{D}(\omega)|^2$, the modulus squared of the Fourier transform of the dipole velocity (as opposed to that of the dipole acceleration), is the definition of the spectral intensity adopted throughout this work. Solutions to the stationary action condition $d\phi(t)/dt = 0$ are denoted $t[\omega]$. For brevity, we use $\tau[\omega]$ to denote $\tau(t(\omega))$ and likewise for the other quantities which are dependent on the recombination time t.

Below cutoff, short and long trajectories are distinct and a second-order SPA applies; the result is

$$\tilde{D}(\omega) = \left(\frac{i}{\phi''[\omega]}\right)^{1/2} a[\omega]\exp(i\phi[\omega]). \tag{5}$$

Note that the primes indicate derivatives with respect to time, i.e., $\phi'[\omega] = d\phi(t)/dt$ evaluated at $t[\omega]$. Through manipulation of the classical recollision equations, the second derivative of the phase may be shown to equal

$$\phi''(t) = -\frac{d\omega(t)}{dt} = \frac{v(t)[v(t) + E(t)\tau(t)]}{\tau(t)}. \tag{6}$$

The spectral intensity is therefore inversely proportional to the attosecond linear chirp $-d\omega(t)/dt$, which may be simply evaluated given the recombination velocity, electric field at recombination, and trajectory duration.

Around recombination times $t \approx t[\omega_c]$ corresponding to the cutoff frequency ω_c, the phase $\phi(t)$ has a cubic shape, and a third-order SPA is necessary. To obtain the same level of accuracy as the second-order SPA combined with the uniform approximation, the first-order behavior of the slowly varying amplitude $a(t)$ must be considered at the cutoff. The resulting expression is of similar form to the uniform approximation, and is deferred until Sec. III. However, by taking $a(t)$ as constant around the cutoff, a simpler expression for the amplitude, which contains all the scaling factors, is obtained:

$$\tilde{D}(\omega_c) = \frac{\sqrt{2\pi}}{3^{2/3}\Gamma(2/3)}\left(\frac{2}{\phi'''[\omega_c]}\right)^{1/3} a[\omega_c]\exp(i\phi[\omega_c]). \tag{7}$$

The third derivative $\phi'''(t)$ of the action is the attosecond quadratic chirp $-d^2\omega(t)/dt^2$. At the cutoff, the following analytic expression follows from the recollision equations:

$$\left.\frac{d^2\omega(t)}{dt^2}\right|_{t=t[\omega_c]} = \frac{E(t)\{E(t)[E_b(t) - E(t)] + \tau E'(t)E_b(t)\}}{E_b(t)}, \tag{8}$$

where $E_b(t) = E(t_b(t))$ for brevity.

Equations (5) and (7) contain all the scaling mechanisms discussed throughout this paper. However, as mentioned above they do not smoothly cover the coalescence of the long and short trajectories, nor do they describe frequencies above the cutoff. For the calculation of complete harmonic spectra, one needs to employ the uniform approximation, which is presented in the next section.

III. UNIFORM APPROXIMATIONS APPROACHING THE CUTOFF AND BEYOND

This section derives the form of the uniform approximation [24] used to calculate the combined amplitude of the long and short trajectories at harmonic frequencies approaching the cutoff from below, as well as a form valid for the cutoff and above. Previous applications of the uniform approximation to high-harmonic generation [25] and above-threshold ionization [26] have treated the case of complex-valued birth and return times which arise when the stationary phase condition at birth is solved exactly, i.e., $v(t_b)^2/2 + I_p = 0$. In this situation, the two saddle points do not intersect, and methods of contour integration are required. Here, we use the stationary phase condition $v(t_b) = 0$. Although the final result for the uniform approximation is similar to the complex-valued case, there are some differences in the derivation and so we present it here.

In the uniform approximation, one rewrites the Fourier transform integral Eq. (4) such that it takes the form of Airy's integral, which involves a cubic phase function, but reduces exactly to the sum of two second-order SPAs when the stationary points are far apart. An appropriate form is

$$\tilde{D}(\omega) \approx \sqrt{2u}\int\left[\bar{a}_+ + \frac{\bar{a}_-}{u}t'\right]\exp\left[i\left(\frac{t'^3}{3} - u^2t' + \phi_+\right)\right]dt', \tag{9}$$

where

$$\bar{a}(t) = \frac{a(t)}{\sqrt{2\pi\phi''(t)}}, \quad u = \left(\frac{3\phi_-}{2}\right)^{1/3}, \tag{10}$$

$$2\bar{a}_+ = \bar{a}(t_1) + \bar{a}(t_2), \quad 2\bar{a}_- = \bar{a}(t_1) - \bar{a}(t_2), \tag{11}$$

$$2\phi_+ = \phi(t_1) + \phi(t_2), \quad 2\phi_- = \phi(t_2) - \phi(t_1). \tag{12}$$

Here t_1 and t_2 are the two stationary points of the phase, labeled such that $\phi(t_2) > \phi(t_1)$, i.e., $\phi_- > 0$. The phase in Eq. (9) has stationary points at $t' = \pm u$. The pre-exponential factor in Eq. (9) varies linearly from $\bar{a}(t_2)$ to $\bar{a}(t_1)$ between the stationary points. Scaling $a(t)$ by the inverse square root of its second derivative ensures that applying the SPA to Eq. (9) recovers the sum of the second-order SPAs Eq. (5) for the two trajectories. However, Eq. (9) may also be evaluated exactly using Airy functions to yield

$$\tilde{D}(\omega) \approx 2\pi\sqrt{2u}\left[\bar{a}_+\mathrm{Ai}(-u^2) - \frac{i\bar{a}_-}{u}\mathrm{Ai}'(-u^2)\right]e^{i\phi_+}. \tag{13}$$

Application of Eq. (13) to Eq. (4) therefore provides a convenient way of evaluating the dipole amplitude which smoothly covers all of the plateau.

Approaching the cutoff where the roots coalesce, numerical errors begin to limit the accuracy of the finite differences $\bar{a}_-$ and $\bar{\phi}_-$, and one must switch to a method which explicitly includes the third derivative of the phase and, to obtain the same order of accuracy as the uniform approximation, the first-order variation of $a(t)$. The integral to be evaluated is therefore

$$\tilde{D}(\omega) \approx (2\pi)^{-1/2}\int[a_0 + a_1t]\exp\left[i\left(\phi_0 + \phi_1t + \frac{\phi_3t^3}{6}\right)\right]dt, \tag{14}$$

where a_n and ϕ_n are the nth-order derivatives of $a(t)$ and $\phi(t)$ at the cutoff recombination time, here denoted t_0. Equation (14) may again be evaluated using Airy functions; the result is

$$\tilde{D}(\omega) \approx b\sqrt{2\pi}[a_0\mathrm{Ai}(x) - ia_1b\mathrm{Ai}'(x)]\exp(i\phi_0), \tag{15}$$

where $b = (2/\phi_3)^{1/3}$ and $x = \phi_1b$. We shall refer to Eq. (15) as the augmented third-order stationary phase approximation; by ignoring the first-order dependence of the integrand, i.e., setting $a_1 = 0$, we obtain the third-order stationary phase approximation. The difference is of order 0.1% for the cases studied here. At the cutoff, $\phi_1 = 0$ and using the third-order stationary phase approximation we obtain Eq. (7).

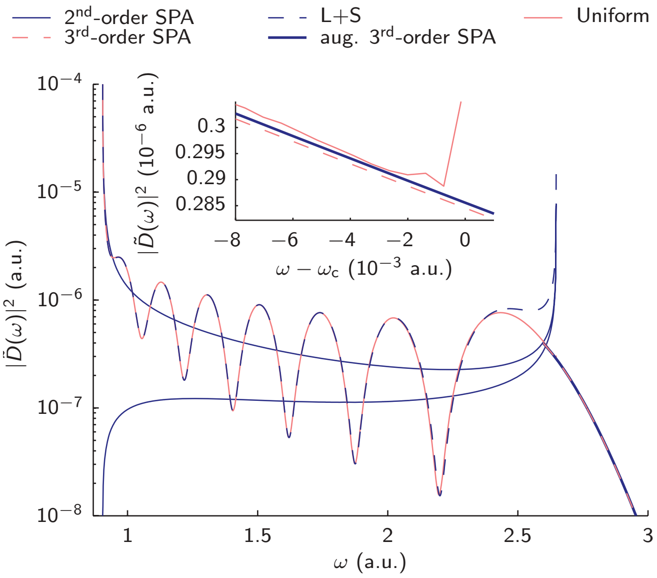

FIG. 2. (Color online) Comparison of the various stationary phase approximations to the spectral intensity for $\lambda_L = 566$ nm. Below the classical cutoff at $\omega_c = 2.64$ a.u., second-order stationary phase approximations are shown for short and long trajectories (thin dark blue solid lines), sum of long and short contributions (thin dark blue dashed line), and uniform approximation (thin light red solid line). Above the cutoff, third-order stationary phase approximations are shown with (thick dark blue solid line) and without (thin light red dashed line) first-order behavior of the integrand. Inset: zoomed-in view around the cutoff.

The results of the various approximations for $\lambda_L = 0.56\,\mu$m are shown in Fig 2. The second-order stationary phase approximations for the long and short trajectories, given by Eq. (5) and shown as solid dark blue lines, diverge at the cutoff. Their sum, shown as a dashed dark blue line, exhibits quantum path interference but also diverges at the cutoff. The uniform approximation, given by Eq. (13) and shown as a solid light red line, agrees with the individual trajectory results below the cutoff but does not diverge. Above the cutoff, the third-order stationary phase approximations, given by Eq. (15), continue on from the uniform approximation.

The inset shows a zoomed-in view around the cutoff which illustrates the typical behavior of the different approximations. The uniform approximation smoothly connects with the augmented third-order stationary phase approximation, shown as a thick dark blue line. However, because the uniform approximation requires two distinct roots, numerical errors arise approaching the cutoff from below. Therefore, some judgment is required in choosing the transition frequency. The third-order SPA, shown as a dashed light red line, does not connect with the uniform approximation, even with perfect numerical accuracy.

IV. COMPARISON BETWEEN SFA AND TDSE

To verify the accuracy of the analytic results of the previous two sections, we performed a set of TDSE calculations with a laser of intensity 5×10^{14} W/cm^2 and with wavelength varying over the range 566–2263 nm. The temporal profile was a 1.5 cycle flat-top pulse, proportional to $\cos(\omega_L t)$ in the interval $-\pi/(2\omega_L) < t < 5\pi/(2\omega_L)$ and zero elsewhere. We thereby obtained the response from electrons born during a single laser half cycle. The atomic potential was of a helium atom shielded by the 1s state:

$$V(r) = -\frac{1}{r}\left[1+\left(\frac{2r}{a}+1\right)\exp\left(-\frac{4r}{a}\right)\right], \qquad (16)$$

where $a = 1.184$ a.u. to give a matching ionization potential. We applied temporal windows to the dipole velocity to separate the contributions from the long and short trajectories. We used a cylindrical coordinate system with rotational symmetry about the laser polarization.

For spatial discretization we used the second-order finite differencing scheme with carefully softened Coulomb potential given in Ref. [27]. We used a perfectly matched layer [28,29] to truncate the mesh, which provided substantial improvements in computational efficiency, particularly in the direction transverse to the laser polarization where imaginary absorbing potentials would have caused significant reflections of the diffracting wave packet. Temporal integration was performed using the split-operator method. All results were checked for convergence in the grid size, the mesh truncation distance, and the damping parameter of the perfectly matched layer.

Figure 3(a) compares the spectrum, decomposed into short, long, and cutoff contributions, from the TDSE and SFA for a drive wavelength of 2263 nm. The agreement, for both long and short trajectories, is excellent down to photon energies of just a few multiples of the ionization potential. The oscillations in the TDSE spectra are artifacts of the temporal windowing used to isolate the trajectories. The gap just below the cutoff in the SFA spectrum is an artifact of the trajectory separation and is removed by the uniform approximation. Figure 3(b) presents the same information for a drive wavelength of 566 nm. Despite having a Keldysh parameter of 0.9, there is agreement in the overall amplitudes to within a factor of 2.

We now present comparisons of the SFA and TDSE results for the drive wavelength scaling. Figure 4(a) shows the spectral intensity as a function of drive wavelength under the FAE condition $\omega = 4$ a.u. (109 eV). There is good agreement between the TDSE and the SFA over the full range of wavelengths and for both trajectories, except for the artifacts around the cutoff

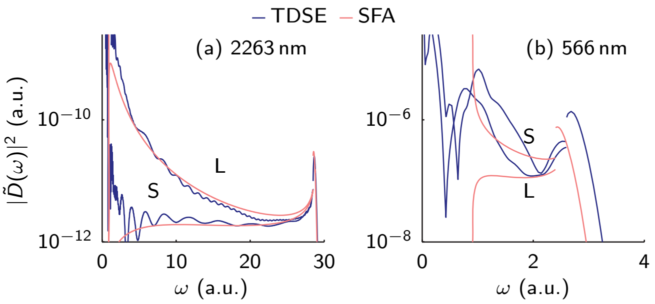

FIG. 3. (Color online) (a) and (b) Harmonic spectrum computed using TDSE (dark blue lines) and SFA (light red lines, second-order SPA below cutoff, augmented third-order SPA above cutoff) with drive wavelength at (a) 2263 nm and (b) 566 nm. The contributions from the long and short trajectories are displayed separately below the cutoff.

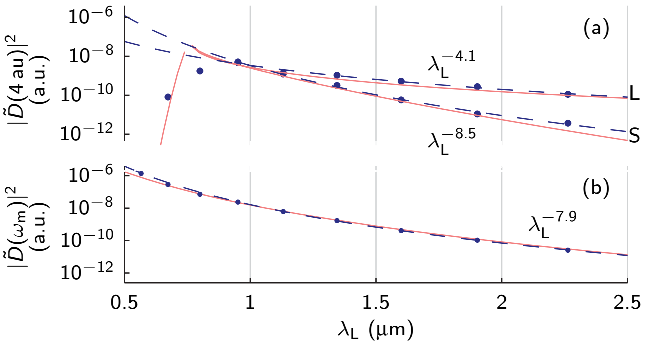

FIG. 4. (Color online) (a) Dipole spectral intensity at harmonic frequency $\omega = 4$ a.u. versus drive wavelength for a single laser half cycle of intensity 5×10^{14} W/cm^2 in helium; SFA (light red solid lines) and TDSE (dark blue dots) for short (S) and long (L) trajectories; power law fits to the TDSE results for $\lambda_L > 800$ nm (dashed dark blue lines). (b) Peak value of the dipole spectral intensity near the cutoff versus drive wavelength, otherwise identical parameters to (a).

which occur at $\lambda_L = 750$ nm. Figure 4(b) shows the maximum spectral intensity around the cutoff—the FRE condition—with good agreement between the TDSE and SFA.

V. SCALING AT FIXED ABSOLUTE ENERGY

Having shown the consistency of the TDSE and the SFA, we now use the latter to examine the wavelength scaling under the FAE condition. The trajectory duration τ, taken by dimensional arguments to scale as λ_L, is plotted for $\omega = 4$ a.u. in Fig. 5(a). The duration of the long trajectory increases slightly faster than the drive wavelength, and the short trajectory increases much less rapidly, in concordance with point 1 made in the Introduction. We conclude that trajectory lengthening is much less significant for the short trajectories than previously believed.

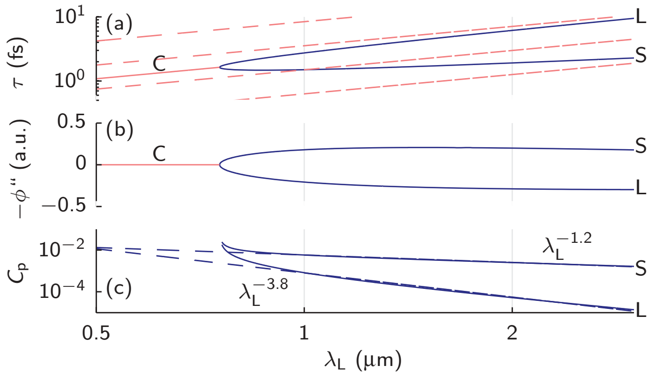

FIG. 5. (Color online) Drive wavelength dependence of electron spatial and temporal spreading for short (S, dark blue solid lines), long (L, dark blue solid lines), and cutoff (C, light red solid lines) trajectories; parameters equal to Fig. 4(a). (a) Trajectory duration; lines proportional to λ_L (light red dashed lines) are shown as a guide to the eye. (b) Attosecond linear temporal chirp. (c) Full scaling due to wave-packet spreading and attosecond chirp with power-law fits for $\lambda_L > 800$ nm (dashed dark blue lines).

The attosecond linear chirp ϕ'', taken from dimensional analysis to scale linearly with λ_L [6,14], is plotted versus drive wavelength in Fig. 5(b) and in fact increases in magnitude rapidly from zero at the cutoff to a near-constant value for both long and short trajectories. This is explained through consideration of the self-similar shape of the attosecond burst in the (ω,t_r) domain [30], the slope of which is the attosecond linear chirp. Relative to the cutoff, the point of emission moves to lower harmonic frequencies where the slope is lower, counteracting the overall horizontal and vertical stretching with drive wavelength which forms the dimensional argument.

Combining the effects of the trajectory duration and the attosecond chirp, we obtain the full scaling $C_p = (2\pi/\tau)^3|\phi''|^{-1}$ associated with wave-packet dynamics of the continuum electron in the plateau. It is plotted in Fig. 5(c) for the long and short trajectories, along with power-law fits for $\lambda_L > 800$ nm. The long trajectory has stronger scaling as expected from the trajectory durations, which give the main contribution to C_p: $\lambda_L^{-1.2}$ and $\lambda_L^{-3.8}$ for the short and long trajectories, respectively. For the long trajectory the continuum wave-packet effects nearly reproduce the numerically observed scaling in Fig. 4(a). However, their influence upon the short trajectory is a factor of $\lambda_L^{-7.3}$ weaker than that which is observed, implying the existence of a strong additional scaling mechanism besides that of continuum wave-packet dynamics. As we will show in the next section, these results are general and apply to any harmonic frequency and laser intensity, with the exponents depending only on the interval chosen for the power-law fits.

We now consider the drive wavelength dependence of the ionization rate at birth. The phase of electron birth for $\omega = 4$ a.u. is plotted in Fig. 6(a). With increasing wavelength, the birth phase of the long trajectory tends slowly towards a peak of the field, whereas that of the short trajectory tends towards $-\pi/2$, i.e., a zero-crossing of the cosinusoidal field. Through its impact on the tunnel ionization rate, this effect has profound consequences for the scaling. Figure 6(b) shows the modulus squared of the launched wave packet [Eq. (3)]. For the long trajectory this quantity decreases slightly with drive wavelength due to the counteracting effects of the slowly increasing electric field and the decreasing

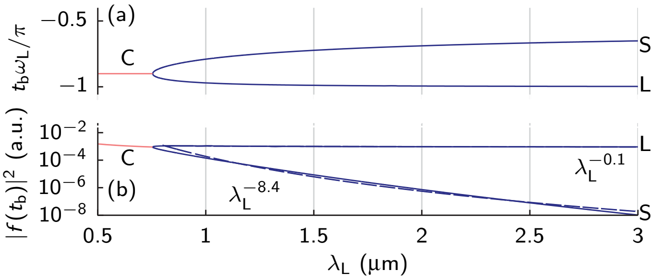

FIG. 6. (Color online) Dependence on drive wavelength of (a) laser field phase at moment of electron birth (in units of π), and (b) amplitude squared of the zero-transverse-momentum component of the launched wave packet for short (S, dark blue solid lines), long (L, dark blue solid lines), and cutoff (C, light red solid lines) trajectories. The dark blue dashed lines show power-law fits for $\lambda_L >$ 800 nm. (For the long trajectory, the power-law fit is indistinguishable from the data at this scale.) The parameters are equal to those of Fig. 4(a).

multiphoton contribution. However, for the short trajectory it drops dramatically, in this case as $\lambda_L^{-8.4}$, due to the extreme sensitivity of tunnel ionization to the instantaneous electric field. This effect is the dominant contribution to the scaling of the short trajectory. We attribute the discrepancy between the observed scaling [Fig. 4(a), $\lambda_L^{-8.5}$] and that predicted by the combination of wave-packet dynamics and the ionization rate [$\lambda_L^{-(1.2+8.4)}$] to the effect of the cutoff and imperfect modeling of the ionization rate, both in the analytics and in the TDSE model atom. As an aside, the significant role of the subcycle ionization rate suggests that careful yield comparisons between different wavelengths will constrain models of strong-field ionization.

VI. UNIVERSAL SCALING DUE TO CONTINUUM WAVE-PACKET DYNAMICS

The previous section examined the FAE scaling for the particular case of the harmonic at $\omega = 4$ a.u. with a laser field of 5×10^{14} W/cm^2. In this section we attempt to generalize this result where possible. In particular, we show that the scaling factors due to continuum wave-packet dynamics, i.e., wave-packet spreading and attosecond chirp, can be expressed in terms of normalized functions which are universal for all frequency and amplitude scalings of a given electric-field profile (e.g., a sinusoid). We use an overbar to denote values for the scaled case $\omega_L = E_L = 1$. For example, $E(t) = E_L\bar{E}(\bar{t})$ where $\bar{t} = \omega_L t$. For the analytical results, the scaled field profile remains arbitrary, although we focus on the sinusoidal field case when discussing the results. The ionization rate, recombination element, and ground-state amplitudes depend on the details of the atom, and in general such a factorization will not be possible. However, for the factors arising from the continuum, one obtains $\tau = \bar{\tau}/\omega_L$, $\phi'' = E_L^2\bar{\phi}''/\omega_L$, and $\phi''' = E_L^2\bar{\phi}'''$. The product of continuum-related scaling factors, introduced in the previous section, therefore scales as $C_p = \omega_L^4 E_L^{-2}\bar{C}_p$, $\bar{C}_p = (2\pi/\bar{\tau})^3|\bar{\phi}''|^{-1}$ in the plateau, and $C_c = \omega_L^3 E_L^{-4/3}\bar{C}_c$, $\bar{C}_c = (2\pi/\bar{\tau})^3|\bar{\phi}'''|^{-2/3} = 3.48$ at the cutoff. The laser frequency and amplitude factors in C_p and C_c lead to the dimensional arguments for the yield scaling, whereas $\bar{C}_p$ incorporates the effect of changing timings with respect to the optical cycle. Figure 7(a) shows $\bar{C}_p$ plotted as a function of the relative photon energy $\bar{\omega} = (\omega - I_p)/U_p$. Across the range $0.5 < \bar{\omega} < 2.5$, $\bar{C}_p$ decreases approximately tenfold for the short trajectories and approximately doubles for the long trajectories.

We now obtain an expression for the overall wave-packet-related scaling C_p which makes explicit the drive wavelength scaling under the FAE condition. We define ω_{LC} and λ_{LC} as the laser frequency and wavelength which at laser amplitude E_L result in ω being at the cutoff. Then, we have

$$C_p = \bar{K}_p(\omega_L/\omega_{LC})\omega_{LC}^4 E_L^{-2}, \qquad (17)$$

where $\bar{K}_p(\epsilon) = \bar{C}_p(\bar{\omega}_C\epsilon^2)\epsilon^4$ and $\bar{\omega}_C = 3.17$ is the normalized harmonic frequency at cutoff. Similar to $\bar{C}(\omega)$, the function $\bar{K}(\epsilon)$ incorporates the influence of the subcycle trajectory timings on the continuum wave-packet dynamics but is expressed in terms of the ratio $\epsilon = \omega_L/\omega_{LC}$ of the laser frequency to that which would result in the harmonic in question being at cutoff. It is plotted against $\epsilon^{-1} = \lambda_L/\lambda_{LC}$ in Fig. 7(b) and is in fact just a scaled and normalized version of Fig. 3(c). (The differences in the exponents of the power fits are due to a different fitting interval.) This illustrates that the analysis of continuum wave-packet effects (but not of ionization rates) is generally applicable to different laser wavelengths and intensities and all field profiles which are sufficiently close to sinusoidal.

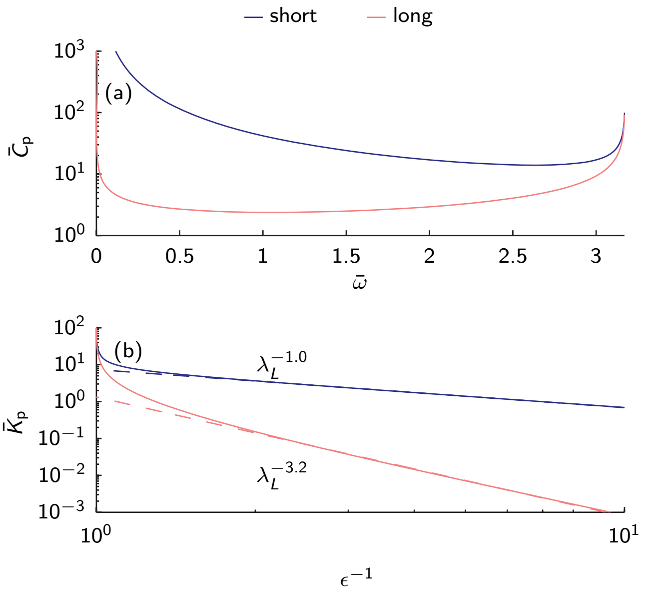

FIG. 7. (Color online) (a) Normalized continuum wave-packet scaling factors for short (dark blue solid lines) and long (light red solid lines) trajectories (a) as a function of normalized frequency $\bar{\omega}$ and (b) as a function of the ratio of laser wavelength to that which results in cutoff, $\epsilon^{-1} = \lambda_L/\lambda_{LC}$. Power-law fits are shown for $2 < \epsilon^{-1} < 10$ (dashed lines).

VII. SCALING AT FIXED RELATIVE ENERGY

We now consider the scaling under the FRE condition, in which the trajectory duration and attosecond chirp scale according to dimensional analysis. Their contribution to the response therefore goes as λ_L^{-3} in the cutoff and λ_L^{-4} in the plateau. The birth phase is constant, and hence so is the tunnel ionization rate. The only other factor is the recombination amplitude. The conversion from acceleration to velocity gives an additional λ_L^{-4} scaling of the response for $U_p \gg I_p$, resulting in a total of λ_L^{-7} and λ_L^{-8} in the cutoff and plateau, respectively [14]. However, the acceleration matrix element also varies with frequency for the atoms (He, Ne) and photon energies (50–2000 eV) of interest. In our model atom, this brings the total SFA scaling in the cutoff to $\lambda_L^{-7.6}$—close to the TDSE result in Fig. 4(b). In reality, the recombination amplitude is an open research topic, particularly with regard to multiple-electron effects [31] and the use of exact photorecombination cross sections [32]. However in the single-electron picture and using the plane-wave (first Born) approximation, customarily used with the SFA, a general statement is possible here. The Coulomb singularity dominates the dipole acceleration dipole matrix element [33] and goes as v^{-1} for high momenta. Therefore, while atom-specific behavior is seen at lower photon energies, the element reaches a maximum—at 45, ≈250, and ≈450 eV for H, He, and Ne, respectively [14]—and then tends towards an $\omega^{-1/2}$ decay in amplitude. Through the $\approx\lambda_L^2$ dependence of the cutoff, it therefore adds a λ_L^{-2} scaling to the intensity in the high photon energy limit. The product of the contributions from wave-packet spreading (λ_L^{-3}), the conversion from the acceleration matrix element to the dipole velocity (λ_L^{-4}), and the acceleration matrix element itself (λ_L^{-2}) gives λ_L^{-9} in the high photon energy limit.

VIII. CONCLUSION

In summary, the drive wavelength scaling of the single-atom response at constant photon energy and laser intensity is influenced by the changing timing of the trajectories with respect to the optical cycle. This point resolves the discrepancy between the SFA and the TDSE. The SFA predicts that the yield at the cutoff scales as λ_L^{-9} in the limit of high photon energy and assuming dominance of the Coulomb singularity in the recombination amplitude. Incorporating these single-atom results into macroscopic models will assist the design of laser-driven sources of bright ultrashort x rays and enable more straightforward comparisons between theory and experiment.

ACKNOWLEDGMENTS

We acknowledge partial support from the Spanish Ministry of Education and Science (Consolider Science Program SAUUL CSD 2007-00013 and Plan Nacional FIS2008-06368-C02-01) and from LASERLAB-EUROPE Grant No. 228334. D.R.A. acknowledges support from a Marie Curie Intra-European Fellowship (Project No. 276556-BAXHHG).

[1] P. B. Corkum, Phys. Rev. Lett. **71**, 1994 (1993).
[2] T. Ditmire, E. T. Gumbrell, R. A. Smith, J. W. G. Tisch, D. D. Meyerhofer, and M. H. R. Hutchinson, Phys. Rev. Lett. **77**, 4756 (1996).
[3] M. Hentschel, R. Kienberger, C. Spielmann, G. A. Reider, N. Milosevic, T. Brabec, P. Corkum, U. Heinzmann, M. Drescher, and F. Krausz, Nature (London) **414**, 509 (2001).
[4] T. Ditmire, K. Kulander, J. Crane, H. Nguyen, and M. Perry, J. Opt. Soc. Am. B **13**, 406 (1996).
[5] I. P. Christov, J. Zhou, J. Peatross, A. Rundquist, M. M. Murnane, and H. C. Kapteyn, Phys. Rev. Lett. **77**, 1743 (1996).
[6] A. Gordon and F. Kärtner, Opt. Express **13**, 2941 (2005); V. S. Yakovlev, M. Ivanov, and F. Krausz, *ibid.* **15**, 15351 (2007).
[7] M.-C. Chen, P. Arpin, T. Popmintchev, M. Gerrity, B. Zhang, M. Seaberg, D. Popmintchev, M. M. Murnane, and H. C. Kapteyn, Phys. Rev. Lett. **105**, 173901 (2010).
[8] G. Doumy, J. Wheeler, C. Roedig, R. Chirla, P. Agostini, and L. F. DiMauro, Phys. Rev. Lett. **102**, 093002 (2009).
[9] E. Constant, D. Garzella, P. Breger, E. Mével, C. Dorrer, C. Le Blanc, F. Salin, and P. Agostini, Phys. Rev. Lett. **82**, 1668 (1999).
[10] J. Tate, T. Auguste, H. G. Muller, P. Salières, P. Agostini, and L. F. DiMauro, Phys. Rev. Lett. **98**, 013901 (2007).
[11] K. Schiessl, K. L. Ishikawa, E. Persson, and J. Burgdörfer, Phys. Rev. Lett. **99**, 253903 (2007).
[12] A. D. Shiner, C. Trallero-Herrero, N. Kajumba, H.-C. Bandulet, D. Comtois, F. Légaré, M. Giguère, J.-C. Kieffer, P. B. Corkum, and D. M. Villeneuve, Phys. Rev. Lett. **103**, 073902 (2009).
[13] M. Lewenstein, P. Balcou, M. Y. Ivanov, A. L'Huillier, and P. B. Corkum, Phys. Rev. A **49**, 2117 (1994).
[14] E. L. Falcão-Filho, V. M. Gkortsas, A. Gordon, and F. X. Kärtner, Opt. Express **17**, 11217 (2009). Note that this work uses an alternative definition—the difference is a factor of λ_L^{-2} which we have accounted for here.
[15] M. V. Frolov, N. L. Manakov, and A. F. Starace, Phys. Rev. Lett. **100**, 173001 (2008).
[16] B. Shan and Z. Chang, Phys. Rev. A **65**, 011804 (2001).
[17] J. A. Pérez-Hernández, L. Roso, and L. Plaja, Opt. Express **17**, 9891 (2009).
[18] S. Baker, J. Robinson, C. Haworth, H. Teng, R. Smith, C. Chirila, M. Lein, J. Tisch, and J. Marangos, Science **312**, 424 (2006).
[19] C. I. Blaga, J. Xu, A. D. DiChiara, E. Sistrunk, K. Zhang, P. Agostini, T. A. Miller, L. F. DiMauro, and C. D. Lin, Nature (London) **483**, 194 (2012).
[20] O. Smirnova, Y. Mairesse, S. Patchkovskii, N. Dudovich, D. Villeneuve, P. Corkum, and M. Y. Ivanov, Nature (London) **460**, 972 (2009).
[21] A. Gordon and F. X. Kärtner, Phys. Rev. Lett. **95**, 223901 (2005).
[22] G. L. Yudin and M. Y. Ivanov, Phys. Rev. A **64**, 013409 (2001).
[23] J. C. Baggesen and L. B. Madsen, J. Phys. B: At., Mol. Opt. Phys. **44**, 115601 (2011); R. P. Feynman, R. B. Leighton, and M. Sands, in *The Feynman Lectures on Physics*, Vol. 1 (Addison Wesley, Boston, 1964), Chap. 30 .
[24] R. Wong, *Asymptotic Approximations of Integrals* (SIAM, Philadelphia, 2001); O. Vallée and M. Soares, *Airy Functions and Applications to Physics* (World Scientific, Singapore, 2004).
[25] D. B. Milošević and W. Becker, Phys. Rev. A **66**, 063417 (2002).
[26] C. Figueira de Morisson Faria, H. Schomerus, and W. Becker, Phys. Rev. A **66**, 43413 (2002).
[27] A. Gordon, C. Jirauschek, and F. X. Kärtner, Phys. Rev. A **73**, 042505 (2006).
[28] J.-P. Berenger, J. Comput. Phys. **114**, 185 (1994).
[29] A. Ahland, D. Schulz, and E. Voges, Phys. Rev. B **60**, 043413 (1999).
[30] S. Kazamias and P. Balcou, Phys. Rev. A **69**, 063416 (2004).
[31] A. D. Shiner, B. E. Schmidt, C. Trallero-Herrero, H. J. Worner, S. Patchkovskii, P. B. Corkum, J.-C. Kieffer, F. Legare, and D. M. Villeneuve, Nat. Phys. **7**, 464 (2011).
[32] M. V. Frolov, N. L. Manakov, T. S. Sarantseva, and A. F. Starace, Phys. Rev. A **83**, 043416 (2011).
[33] A. Gordon, R. Santra, and F. X. Kärtner, Phys. Rev. A **72**, 063411 (2005).